metals

MDPI

Article

Interplay of C Alloying, Temperature, and Microstructure in Governing Mechanical Behavior and Deformation Mechanisms of High-Manganese Steels

Chenghao Zhang [1], Jinfu Zhao [1], Tengxiang Zhao [1], Ling Kong [1], Chunlei Zheng [2], Haokun Yang [3,*] and Yuhui Wang [1,*]

[1] National Engineering Research Center for Equipment and Technology of Cold Strip Rolling, Yanshan University, Qinhuangdao 066004, China; zhangchenghao@stumail.ysu.edu.cn (C.Z.); zjf@stumail.ysu.edu.cn (J.Z.); zhaotengxiang@stumail.ysu.edu.cn (T.Z.); kongling@ysu.edu.cn (L.K.)
[2] Key State Laboratory of Metastable Materials Science and Technology, Yanshan University, Qinhuangdao 066004, China; zhengclysu@ysu.edu.cn
[3] Smart Manufacturing Division, Hong Kong Productivity Council, Hong Kong 999077, China
* Correspondence: hkyang@hkpc.org (H.Y.); yhwang@ysu.edu.cn (Y.W.)

Abstract

This study investigates the mechanical behavior and deformation mechanisms of Fe-30Mn-0.05C (30Mn0.05C) and Fe-34Mn-0.7C (34Mn0.7C) steels at room temperature (RT) and liquid nitrogen temperature (LNT). The 30Mn0.05C sample exhibited a significant enhancement in both strength and ductility at LNT, achieving a total elongation of 85%. In contrast, the 34Mn0.7C sample demonstrated superior ductility (90%) at RT, with a marginal reduction in plasticity but a remarkable increase in strength (>1100 MPa) at LNT. Compared to the 30Mn0.05C, the 34Mn0.7C, characterized by higher carbon content, displayed more pronounced dynamic strain aging (DSA) effects. Additionally, a greater density of deformation twins was activated at LNT, revealing a strong correlation between deformation twinning and DSA effects. This interplay accounts for the simultaneous strength improvement and ductility reduction observed in the 34Mn0.7C at LNT. Furthermore, the 34Mn0.7C sample exhibited a significantly refined grain structure after rolling, contributing to a substantial strength increase (approaching 1500 MPa) at the expense of ductility. This trade-off can be attributed to the pre-introduction of a higher density of dislocations and deformation twins during rolling, which facilitated strengthening but limited further plastic deformation.

Keywords: dynamic strain aging; high manganese steels; twining; liquid nitrogen temperature; premature fracture

check for updates

Academic Editor: Koh-ichi Sugimoto

Received: 3 June 2025
Revised: 2 July 2025
Accepted: 7 July 2025
Published: 9 July 2025

Citation: Zhang, C.; Zhao, J.; Zhao, T.; Kong, L.; Zheng, C.; Yang, H.; Wang, Y. Interplay of C Alloying, Temperature, and Microstructure in Governing Mechanical Behavior and Deformation Mechanisms of High-Manganese Steels. *Metals* **2025**, *15*, 779. https://doi.org/10.3390/met15070779

Copyright: © 2025 by the authors. Licensee MDPI, Basel, Switzerland. This article is an open access article distributed under the terms and conditions of the Creative Commons Attribution (CC BY) license (https://creativecommons.org/licenses/by/4.0/).

1. Introduction

Single-phase austenitic high-manganese steels, when having a higher C content, such as Fe-18Mn-1.0C, Fe-32Mn-0.6C, and Fe-22Mn-0.6C steels, exhibit a continuous step-like serrated pattern in the tensile flow stress curves when subjected to tensile deformation tests at certain temperatures and strain rates [1,2]. It is known that these serrations are caused by the repeated nucleation and propagation of localized deformation bands in the parallel ends of the specimen during the tensile test [3–6]. This band is referred to as the Portevin-Le Chatelier (PLC) band [7], which is caused by dynamic strain aging (DSA) [8]. DSA in solid solutions is characterized by the diffusion of solute atoms, particularly C, towards mobile dislocations temporarily arrested at obstacles [9]. Caillard's study on Fe-16C (ppm at.%)

demonstrated that DSA in steel arises from dynamic interactions between dislocations and C atoms during deformation, with C concentration playing a pivotal role [10]. Higher C content promotes Mn-C complex formation, enhancing dislocation interactions and DSA effects [11]. The diffusion and pinning of C atoms at dislocations are central to DSA mechanisms [12].

Yang, H.K. et al. [13,14] in their study on Fe-22Mn-0.6C and Fe-22Mn-1.0C steels, evaluated the DSA effect and found that both strength and plasticity were simultaneously enhanced with increasing temperature. Kim et al. [15] observed that in Fe-18Mn-0.6C and Fe-22Mn-0.6C steels, DSA is temperature-dependent, with optimal C diffusion rates enhancing DSA within specific temperature ranges. Grässel et al. [16,17] noted that temperature influences C mobility and dislocation kinetics in austenitic Fe-(15-30)Mn steels, with intermediate temperatures favoring DSA by facilitating C diffusion to dislocations, while extremely low temperatures may alter DSA due to reduced atomic mobility. Strain rate significantly impacts DSA behavior. Renard et al. [18] found that Fe-Mn-1.2C high-Mn austenitic TWIP steels exhibit serrated flow within specific temperature and strain rate ranges. Litovchenko et al. [19]. discovered through mechanical testing of modified reduced-activation austenitic steels over a temperature range of 20–750 °C that distinct serrated flow characteristics were observed in the tensile curves of solution-treated specimens within the 500–600 °C interval, while such features were completely absent in cold-rolled samples. Khedr et al. [20–22] demonstrated that DSA is more pronounced at lower strain rates, where C atoms have sufficient time to diffuse and uniformly surround dislocations, enhancing work hardening but suppressing deformation twinning. Conversely, higher strain rates eliminate DSA due to insufficient time for C diffusion [23,24].

The interaction between dislocations and C atoms, including Cottrell atmosphere formation and dislocation pinning. Partial dislocations locally transform the fcc phase to hcp, shifting C atoms from octahedral to tetrahedral interstitial sites [25], and then C atoms displaced by partial dislocations can revert to octahedral sites, forming Mn-C complexes. In high-Mn steels, partial dislocations and their interaction with C atoms have been proposed as a DSA mechanism [15,26–28]. Oh et al. [28] suggested that DSA results from C diffusion along dislocation lines, where mobile dislocations are immobilized by C atoms diffusing from immobile dislocations. Previous studies on the DSA effect in high-manganese steels have primarily focused on varying single parameters, such as C content, temperature, or microstructure, without systematically addressing their combined influence. To comprehensively understand DSA, this study investigates Fe-30Mn-0.05C and Fe-34Mn-0.7C steels by systematically varying C content, temperature, and microstructure. The aim is to elucidate how C concentration affects Mn-C complex formation and C diffusion to dislocations, evaluate the role of grain boundaries in dislocation pinning and deformation band propagation, and clarify DSA behavior under extreme temperatures. This work provides insights for developing advanced high-strength steels with tailored deformation properties.

2. Materials and Methods

The chemical compositions of the Fe-30Mn-0.05C (30Mn0.05C for short) and Fe-34Mn-0.7C (34Mn0.7C for short) steels used in this experiment are shown in Table 1. The experimental steels were smelted using vacuum induction melting and electroslag remelting. The composition of the experimental steels was determined using an X-ray fluorescence spectrometer (ADVANT XP-381 model, Thermo Fisher Scientific, Basel, Switzerland) and an infrared sulfur-carbon analyzer (CS-8800 model, Jinyibo Instrument Technology Co., Ltd., Wuxi, China).

Table 1. Chemical composition of experimental steels (wt.%).

Steel	C	Mn	Si	Cr	Ni	Fe
30Mn0.05C	0.05	30.2	<0.01	<0.01	<0.01	Bal.
34Mn0.7C	0.7	34.4	<0.01	<0.01	0.19	Bal.

The 30Mn0.05C and 34Mn0.7C steel ingots were subjected to solution treatment at 1100 °C for 4 h, followed by forging at temperatures between 800–1000 °C. The 30Mn0.05C steel was forged into square bars with a cross-section of 12 × 12 mm, while the 34Mn0.7C steel was forged into two parts: square bars with a cross-section of 12 × 12 mm and square slabs 26 mm thick. Subsequently, the 26 mm thick square slabs of 34Mn0.7C steel were solution treated at 1000 °C for 2 h, then rolled to a thickness of 12 mm at 600 °C with a rolling reduction of 54%, and air-cooled to room temperature (labeled as 34Mn0.7C(L)).

Microstructural analysis was conducted using a FEI-Scios field emission scanning electron microscope (SEM) (Hillsboro, OR, USA) equipped with an electron backscatter diffraction (EBSD) detector. The operating voltage for the SEM was 10 kV, while the operating voltage for EBSD was 20 kV. Specimens for EBSD testing were prepared using electrical discharge wire cutting, followed by standard mechanical polishing to remove surface wire cutting marks and scratches. Subsequently, the specimens were electropolished in a mixed solution of 10% (volume fraction) HClO4 + 90% (volume fraction) C_2H_5OH, with a polishing voltage of 30 V for 30 s at a temperature between 0 °C and 25 °C. Samples after electropolishing were also subjected to argon ion polishing. The cross-sectional sample preparation was performed using an ion beam milling system (Model IB-19530CP, JEOL Ltd., Japan) operated at 6.5 kV accelerating voltage with 5 sccm argon flow rate for 5 min polishing duration. The EBSD scanning step size varied depending on the grain sizes (step sizes of 0.05, 0.1, and 1 μm being used, respectively).

Transmission electron microscopy (TEM) observations were performed in the FEI Talos F200X (Hillsboro, OR, USA) operated at an accelerating voltage of 200 kV. The ground TEM thin sections were subjected to electrochemical dual-jet polishing in a solution of 10% (volume fraction) $HClO_4$ + 90% (volume fraction) C_2H_5OH, using a constant voltage of 30 V.

The tensile tests were conducted using a universal testing machine (Model BT2-FA100SH, ZwickRoell GmbH, Germany) equipped with a custom-designed environmental chamber. Tensile specimens with a gauge length of 15 mm, a width of 3 mm, and a thickness of 2 mm were prepared from the annealed plates and rolled plates, respectively. Tensile tests were carried out at an initial strain rate of 10^{-3} s^{-1} at RT and LNT; three specimens were tested for each condition. The in-house developed low-temperature testing system consists of a liquid nitrogen bath chamber and a specialized flat specimen gripping assembly. The testing protocol involves: (1) mounting the sheet specimen in the grips, (2) filling the LN_2 chamber to completely immerse the specimen for 10 min to achieve thermal equilibrium, and (3) conducting the tensile test while maintaining continuous LN_2 immersion throughout deformation. This configuration ensures isothermal testing conditions at the liquid nitrogen boiling point (77 K).

3. Results

3.1. Initial State Microstructure Characterization

The initial microstructures of the 30Mn0.05C and 34Mn0.7C exhibit fully recrystallized, as shown in Figure 1a,c. The microstructure of 34Mn0.7C(L) is characterized by a lamellar structure with the lamellar boundaries approximately parallel to the RD (Figure 1e). The mean grain sizes for the 30Mn0.05C and 34Mn0.7C specimens are 18 μm and 20 μm,

respectively (see Figure 1b,d). The boundary spacing was measured for the GNBs (geometrically necessary boundaries) along the direction perpendicular to the boundaries, and the distributions of measured values are shown in Figure 1f. The average values were 1.3 μm.

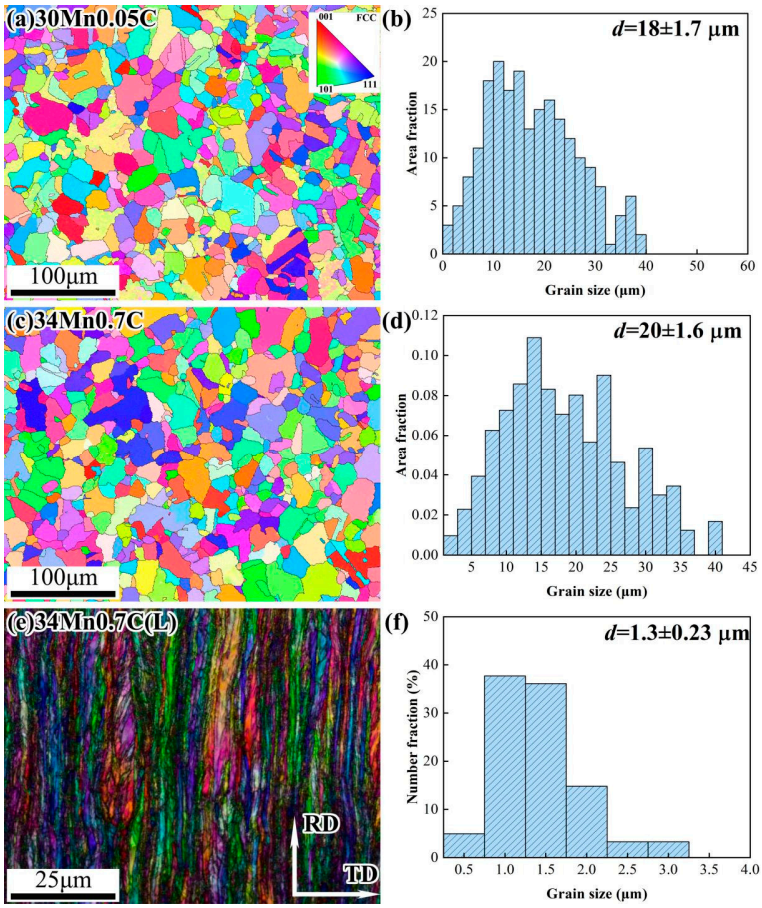


Figure 1. EBSD inverse pole figure (IPF) maps and the corresponding distributions of grain sizes for the (**a**,**b**) 30Mn0.05C, (**c**,**d**) 34Mn0.7C, and (**e**,**f**) 34Mn0.7C(L).

3.2. Tensile Properties and Work-Hardening Behavior

Figure 2 shows the engineering stress-strain curves of 30Mn0.05C, 34Mn0.7C, and 34Mn0.7C(L) specimens under RT and LNT. The engineering stress-strain curves obtained from tensile testing were converted to true stress-strain curves using the standard relationships (true stress $\sigma = \sigma(1 + \varepsilon)$, true strain $\varepsilon = \ln(1 + \varepsilon)$). The work hardening rate (θ) was then calculated as the first derivative of the true stress with respect to true strain ($\theta = d\sigma/d\varepsilon$). This differential processing of the experimentally derived true stress-strain data generated the work hardening rate curves. Table 2 lists the mechanical properties of the three specimens at RT and LNT. The results demonstrate that C content and deformation temperature significantly influence the tensile properties and deformation behavior of the steels. At RT, as shown in Figure 2a, both strength and ductility increase with higher C content. Notably, the RT stress-strain curves of 34Mn0.7C and 34Mn0.7C(L) display pronounced serrations at large strains, indicative of the DSA effect, also known as the Portevin-Le Chatelier (PLC) effect [4]. The intensity of DSA is reflected in the amplitude and spacing of serrations, with denser and larger serrations indicating a stronger effect. Generally, these serrations are characterized by the periodic abrupt rise, followed by a sudden drop to below a general level in the stress-strain curves [29,30]. When the strain increases to approximately 7%, the curve exhibits serrated fluctuations, with the corresponding stress reaching 540 MPa. Another characteristic is that the more pronounced the DSA, the lower the corresponding

strain value at which DSA initiates [10]. At LNT, increasing C content enhances YS and UTS but reduces elongation. Furthermore, no serrations are observed in the stress-strain curves at LNT, suggesting the absence of the DSA effect.

Table 2. Tensile properties of the 30Mn0.05C, 34Mn0.7C, and 34Mn0.7C(L) specimens tested at RT and LNT.

Sample	Temp.	YS (MPa)	UTS (MPa)	UE (%)	TE (%)
30Mn0.05C	RT	241 ± 4.6	530 ± 30.5	40 ± 2.4	49 ± 1.2
	LNT	307 ± 15.6	809 ± 11.9	82 ± 4.7	85 ± 3.2
34Mn0.7C	RT	389 ± 24.8	958 ± 30.6	82 ± 4.7	90 ± 5.5
	LNT	573 ± 11.9	1189 ± 27.7	69 ± 4.8	69 ± 4.7
34Mn0.7C(L)	RT	1087 ± 1.5	1260 ± 2.5	18 ± 1.7	25 ± 1.6
	LNT	1367 ± 23.4	1488 ± 18.5	24 ± 3.6	24 ± 3.6

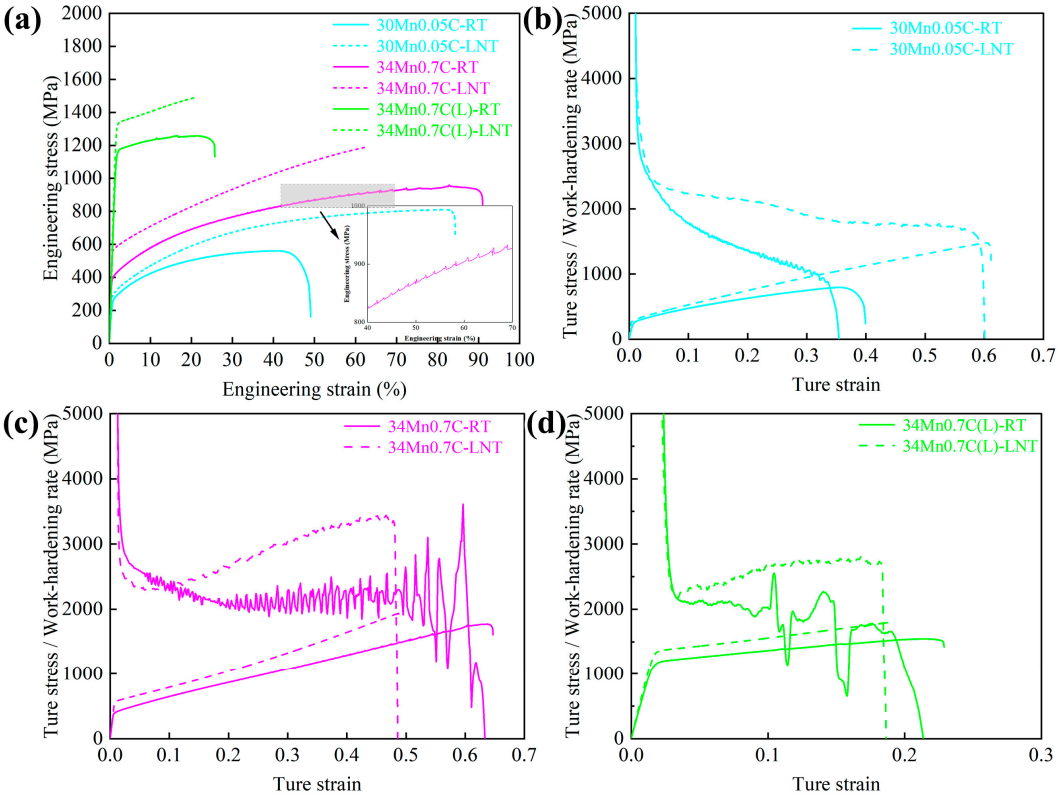


Figure 2. Tensile behavior of the 30Mn0.05C, 34Mn0.7C, and 34Mn0.7C(L) specimens at RT and LNT. (**a**) Engineering stress-strain curves. The inset shows serrations on the curve. (**b**–**d**) Corresponding work-hardening and true stress-strain curves.

Interestingly, as the temperature decreases from RT to LNT, the tensile behavior of 30Mn0.05C, 34Mn0.7C, and 34Mn0.7C(L) specimens exhibits distinct trends. The 30Mn0.05C specimen demonstrates an anomalous temperature dependence, attributed to a transition from dislocation slip-dominated deformation at RT to twinning-dominated deformation at LNT [31,32]. For 30Mn0.05C, the YS increases by ~27% (from 241 MPa to 307 MPa), UTS by ~53% (from 530 MPa to 809 MPa), and TE by ~73.5% (from 49% to 85%). In contrast, for 34Mn0.7C and 34Mn0.7C(L) specimens, strength increases while elongation decreases with temperature reduction. The YS of 34Mn0.7C increases by ~47% (from 389 MPa to 573 MPa), and its UTS by ~24% (from 958 MPa to 1189 MPa), while TE decreases by ~30% (from 90% to 69%). For 34Mn0.7C(L), the YS increases by ~26% (from

1087 MPa to 1367 MPa), and the UTS by ~25% (from 1260 MPa to 1488 MPa), with TE remaining nearly unchanged between RT and LNT.

At LNT, the work hardening rates of 30Mn0.05C, 34Mn0.7C, and 34Mn0.7C(L) specimens significantly increase. Specifically, 30Mn0.05C-LNT exhibits an extended plateau in its work hardening rate before a gradual decline until fracture. In contrast, the work hardening rates of 34Mn0.7C-LNT and 34Mn0.7C(L)-LNT increase steadily but fracture abruptly upon reaching peak values of ~3 GPa and ~3.5 GPa, respectively. According to Considère's criterion for plastic instability ($\sigma \geq d\sigma/d\varepsilon$), instability occurs when the work hardening rate falls below the true stress [3]. Notably, the work hardening curves of all three steels show no drastic fluctuations, further confirming the absence of the DSA effect. Compared to the 30Mn0.05C specimen, both 34Mn0.7C and 34Mn0.7C(L) exhibited DSA effects at RT, with 34Mn0.7C showing a more pronounced DSA effect. However, at LNT, none of the three steels displayed DSA effects. Clearly, C content, temperature, and rolling deformation all have an impact on the DSA effect.

Figure 3 shows the fracture morphologies of 30Mn0.05C, 34Mn0.7C, and 34Mn0.7C(L) specimens under RT and LNT conditions. At RT, the fracture surfaces of both 30Mn0.05C and 34Mn0.7C specimens exhibit small dimples, indicative of typical ductile fracture. Compared to the 34Mn0.7C-RT, the 30Mn0.05C-RT shows a more significant area reduction, as shown in Figure 3a,c. This can be attributed to the higher work hardening rate of the 34Mn0.7C-RT, which delays the early onset of necking instability. The fracture surface of 30Mn0.05C-LNT exhibits a mixed morphology of cleavage facets, dimples, and cracks (Figure 3b), with dimples being smaller and shallower compared to those at RT. In contrast, the primary fracture mode of the 34Mn0.7C specimen at LNT is brittle fracture with intergranular fracture facets, indicating a decrease in plastic deformation capability, as shown in Figure 3d [33]. It is noteworthy that the fracture morphology of 34Mn0.7C(L) is distinctly different from the other two steels, with a large number of secondary cracks appearing in the middle of the fracture surface. The formation of these secondary cracks may be related to the hardness differences between the non-lamellar regions in the steel after rolling. Moreover, there are more secondary cracks at LNT than at RT. This is because dislocation slip is hindered at LNT, leading to a higher likelihood of stress concentration at the lamellar boundaries, which in turn induces the formation of micro-cracks.

3.3. Evolution of Dislocation Density

Figure 4 displays the XRD patterns of the three specimens of 30Mn0.05C, 34Mn0.7C, and 34Mn0.7C(L) after tensile fracture at RT and LNT. It can be observed that the 30Mn0.05C sample exhibits both austenite (FCC) and martensite (HCP) peaks at LNT, whereas the other samples only display austenite peaks at both RT and LNT, indicating that no strain-induced martensitic transformation occurred during deformation. Furthermore, the dislocation density (ρ) is calculated through the following relationship [34–36]:

$$\rho = \frac{3\sqrt{2\pi}\left\langle \varepsilon^2 \right\rangle^{\frac{1}{2}}}{Db} \quad (1)$$

where b and D are the burgers vector and average grain size, respectively. The values of b and D were obtained from the XRD profiles. It can be seen that the dislocation density of the 34Mn0.05C sample is relatively lower than that of the 34Mn0.7C and 34Mn0.7C(L) specimens. Moreover, regardless of whether it is at RT or LNT, the dislocation density generated by the 34Mn0.7C specimen is higher than that of the 34Mn0.7C(L).

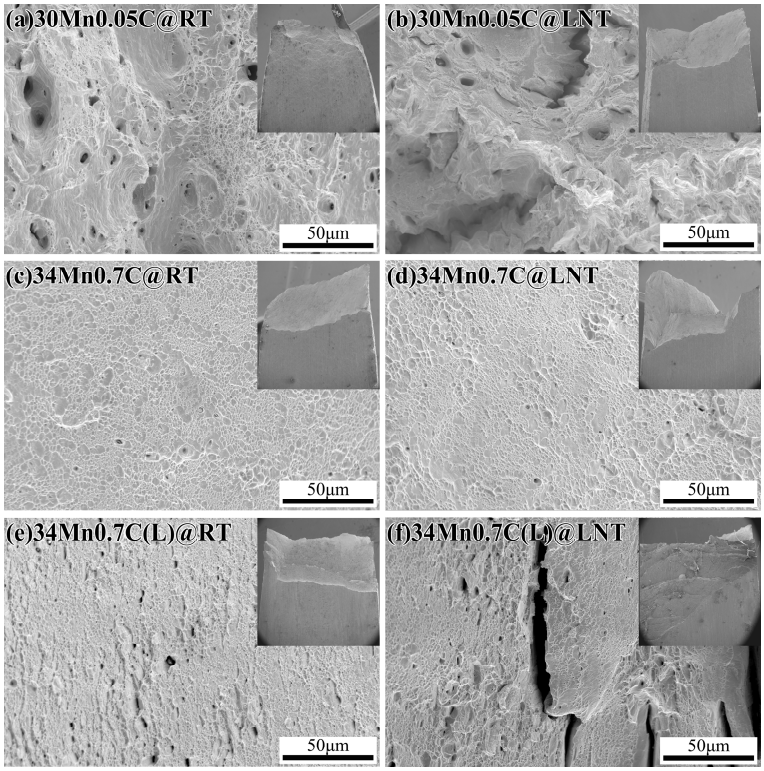


Figure 3. The fracture morphology of the 30Mn0.05C, 34Mn0.7C, and 34Mn0.7C(L) specimens at RT and LNT. (**a**,**c**,**e**) respectively 30Mn0.05C, 34Mn0.7C and 34Mn0.7C at RT. (**b**,**d**,**f**) respectively 30Mn0.05C, 34Mn0.7C and 34Mn0.7C at LNT.

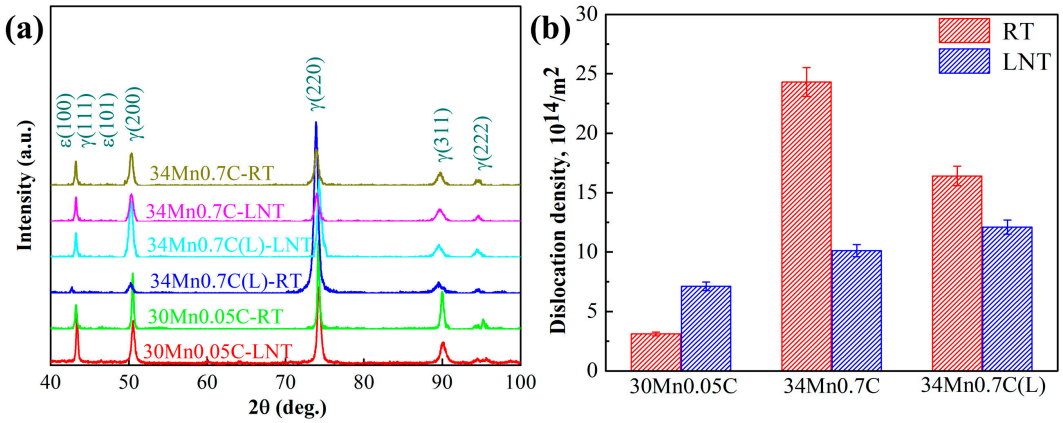


Figure 4. (**a**) X-ray diffraction patterns of the 30Mn0.05C, 34Mn0.7C, and 34Mn0.7C(L) specimens after tensile tests at RT and LNT. (**b**) The measured dislocation density of two steels fractured at RT and LNT.

3.4. Evolution of Deformation Twin

Figure 5 illustrates the combined EBSD maps of IPF and IQ maps, SEM maps, phase diagrams, and corresponding KAM maps of 30Mn0.05C and 34Mn0.7C after tensile deformation at RT and LNT. The fraction of twinned areas in both steels exhibits trends similar to dislocation densities. EBSD maps of 30Mn0.05C in Figure 5a_1,b_1 show no deformation twins at RT, while a limited number of non-penetrating deformation twins and nano-twin bundles are observed at LNT, as highlighted by red arrows and yellow frames in Figure 5b_2. A strain-induced γ(FCC)→ε(HCP) martensitic transformation was identified in the 30Mn0.05C specimen subjected to LNT, as evidenced in Figure 5c_2, where ε-martensite domains (highlighted in red) account for approximately 95% of the microstructure. This quantitative phase distribution is fully consistent with the XRD quantification

results presented in this study. SEM images reveal parallel bands corresponding to twin bundles in EBSD, confirming their identity. Figure 5a$_3$,a$_4$ indicates dense primary and secondary twinning grids at RT, which become sparser at LNT, alongside large twin bundle areas. In contrast, the 34Mn0.7C(L) specimen with a layered structure shows limited EBSD-observable information due to thinner layers (Figure 6). Twins formed during both rolling and tensile deformation are observed within the layers at RT and LNT, necessitating TEM for detailed analysis.

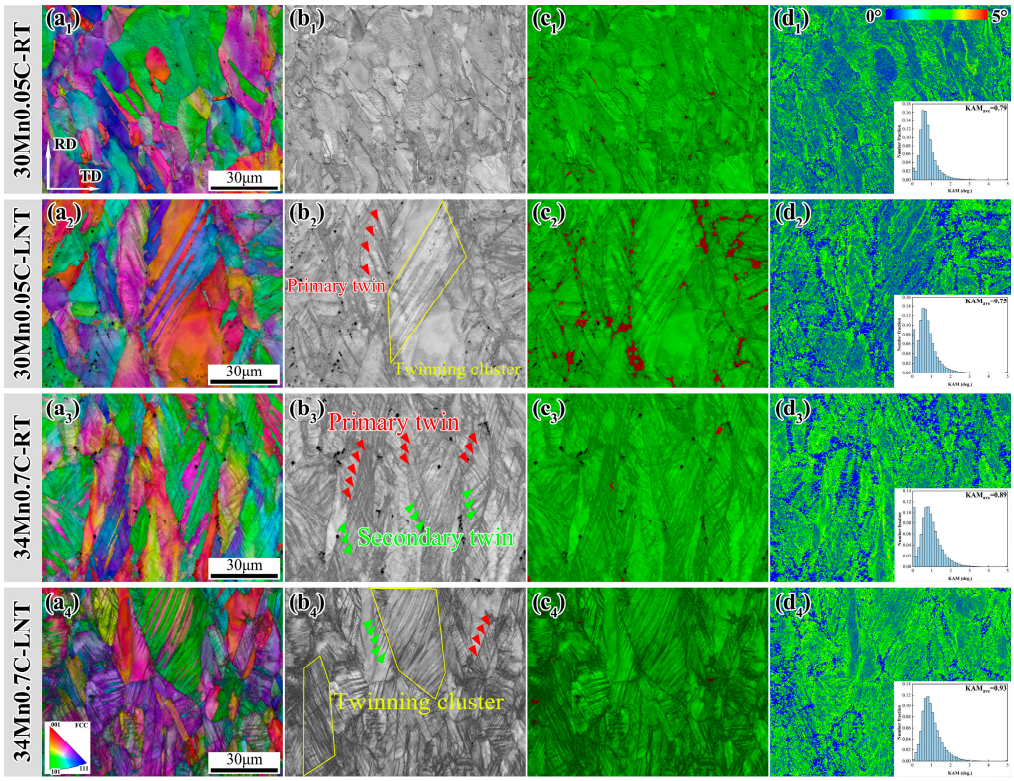


Figure 5. The EBSD analysis of the microstructure. (**a$_1$**–**a$_4$**) IPF+IQ maps, (**b$_1$**–**b$_4$**) SEM maps, (**c$_1$**–**c$_4$**) phase diagrams and (**d$_1$**–**d$_4$**) corresponding KAM maps. (**a$_1$**–**d$_1$**) 30Mn0.05C-RT, (**a$_2$**–**d$_2$**) 30Mn0.05C-LNT, (**a$_3$**–**d$_3$**) 34Mn0.7C-RT, and (**a$_4$**–**d$_4$**) 34Mn0.7C-LNT.

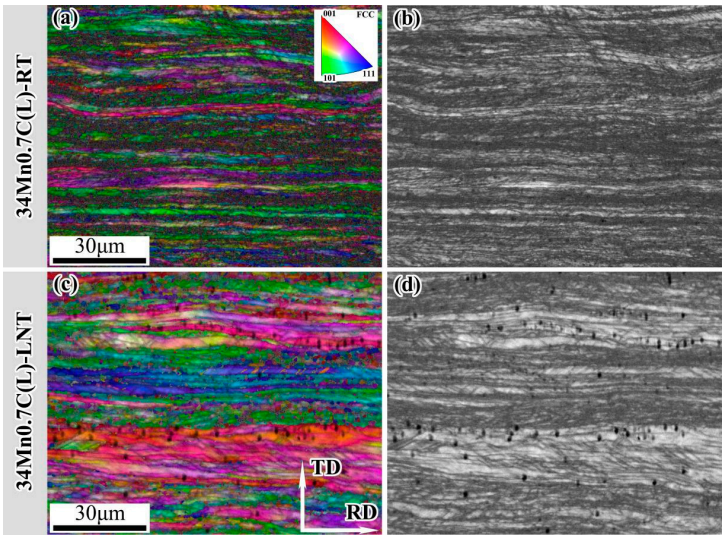


Figure 6. The microstructure of the 34Mn0.7C(L) tensile fracture at RT and LNT. (**a**,**b**) IPF + IQ image and (**c**,**d**) SEM images, (**a**,**c**) at RT, (**b**,**d**) at LNT.

Further microscopic observations of the deformed microstructures of the 30Mn0.05C, 34Mn0.7C, and 34Mn0.7C(L) specimens fractured under RT and LNT conditions were conducted using TEM, as shown in Figures 7–9.

Figure 7 shows the TEM images of the 30Mn0.05C specimens after fracture at RT and LNT. The analysis reveals that the 30Mn0.05C specimen generates fewer deformation twins at LNT compared to RT, and the inter-twin spacing is notably larger. This suggests a reduced tendency for twin formation in the 30Mn0.05C specimen under LNT conditions, which may be attributed to its lower C content and associated microstructural characteristics.

Figure 8 shows TEM images of the 34Mn0.7C specimen after fracture at RT and LNT. Compared to 30Mn0.05C, 34Mn0.7C exhibits a higher density of deformation twins with smaller inter-twin spacing under both temperatures. Twins with different orientations in adjacent grains (Figure 8c) indicate the activation of multiple twin systems, consistent with EBSD observations. The increased twin density and reduced spacing in 34Mn0.7C are attributed to its higher C content, promoting twin nucleation and growth [33]. The diffraction pattern in Figure 8a confirms stacking faults in 34Mn0.7C-RT. At LNT, 34Mn0.7C shows more twin bundles with longer twins and smaller spacing compared to RT, suggesting enhanced twin generation and dislocation interactions under LNT, significantly influencing mechanical properties [37].

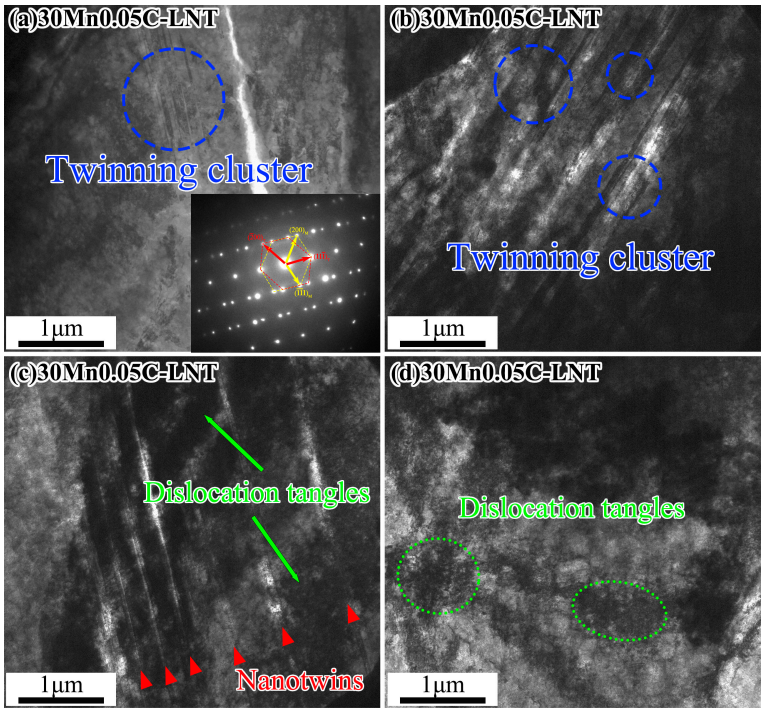


Figure 7. Typical TEM images of 30Mn0.05C after tensile tested at LNT. (**a**) Twining cluster composed of nanotwins formed in the 30Mn0.05C-LNT, fractured, and corresponding selected area electron diffraction pattern (SAEDP) found in the 30Mn0.05C-LNT fractured. (**b**) Twining cluster (**c**) nanotwins and dislocation tangles. (**d**) dislocation tangles in different regions.

Under elevated C content, a higher density of dislocations is generated during deformation, accumulating to form localized stress concentrations that promote the nucleation of deformation twins. Twin boundaries, particularly coherent twin boundaries, act as barriers to dislocation motion, enhancing material strength. At RT, the deformation mechanism is primarily governed by dislocation slip, with limited twin formation due to the lower critical resolved shear stress (CRSS) required for slip compared to twinning [38]. However, twins can accommodate localized strain in regions of stress concentration, such as grain boundaries or dislocation pile-ups. High C content facilitates twin nucleation even at RT

by increasing the stress concentration and reducing the energy barrier for twin formation, enabling a dual deformation mechanism of slip and twinning. This dual mechanism balances high plasticity and moderate strength, particularly in fine-grained or high-strain-rate conditions [22,25].

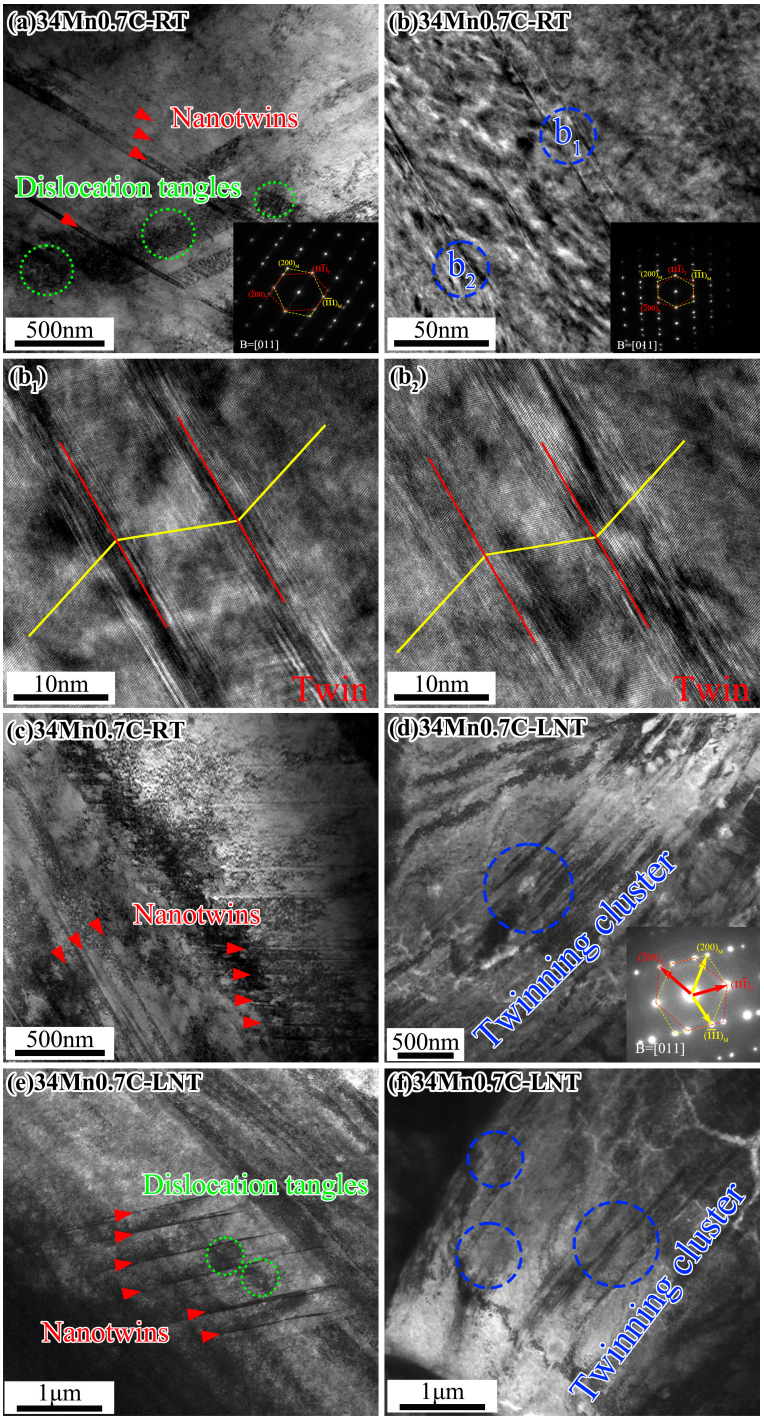


Figure 8. TEM characterization of 34Mn0.7C after tensile tested at RT and LNT. (**a**,**b**) BF and SAED images of nanotwins in 34Mn0.7C-RT specimen, (**b$_1$**,**b$_2$**) the HRTEM images of nanotwins in 34Mn0.7C-RT specimen, with red lines demarcating twin boundaries (TBs) and yellow regions indicating the austenitic matrix orientation, (**c**) primary twin and secondary twin in 34Mn0.7C-RT specimen, (**d**–**f**) BF and SAED images of nanotwins, dislocation tangles, and twinning cluster in 34Mn0.7C-LNT specimen.

At LNT, the plastic deformation mechanism of high-manganese steel shifts significantly, with a pronounced increase in deformation twinning. This transition is driven by the elevated CRSS for dislocation slip and the relatively reduced CRSS for twinning, making twinning the dominant deformation mode. Dislocation activity is restricted, and its contribution to plastic strain is minimized. Deformation twins refine the grain structure by introducing twin boundaries, which act as barriers to dislocation motion, leading to dislocation accumulation near these boundaries. Localized stress concentrations from dislocation pile-ups further promote twin nucleation, creating a dynamic interaction between twinning and dislocations [18,20]. This interplay enhances strain hardening, as twin boundaries impede dislocation glide and promote dislocation storage. Consequently, the strength is significantly enhanced through twin boundary strengthening, while twinning-induced work hardening capacity effectively delays necking and improves ductility [33].

The refinement of twins, characterized by reduced thickness and closer spacing, is driven by the intensified interaction between C atoms and dislocations under high C content. C atoms pin dislocations, increasing local stress for twin nucleation and promoting a higher density of twins, while simultaneously suppressing twin growth by restricting dislocation motion and inhibiting twin boundary expansion. This results in a refined twin morphology that enhances material strength through additional barriers to dislocation motion and maintains plasticity via a dense twin network, enabling coordinated deformation.

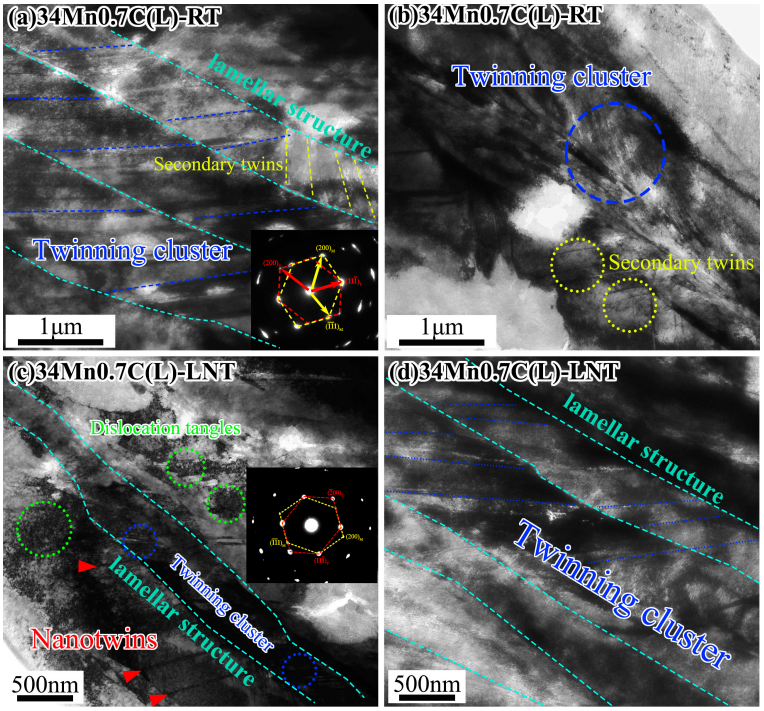


Figure 9. TEM characterization of 34Mn0.7C(L) after tensile tested at RT and LNT. (**a**,**b**) 34Mn0.7C(L)-RT specimen, (**c**,**d**) 34Mn0.7C(L)-LNT specimen, (**a**) BF and SAED images of nanotwins and primary twin and secondary twin, (**b**) twinning cluster and secondary twins, (**c**) BF and SAED images of nanotwins and dislocation tangles, (**d**) twinning cluster.

Figure 9 shows the TEM image of the 34Mn0.7C(L) specimen after fracture. As evident from the micrograph, a substantial number of deformation twins, including secondary twins and twin bundles that continuously traverse the lamellar structure, have formed within the rolled lamellar microstructure. These twins comprise both those introduced during the rolling process and those generated during the subsequent tensile deformation. In comparison to the fully recrystallized specimens, the specimen of lamellar structure exhibits a significantly higher density and quantity of twins. The pre-existing dislocations

and twins introduced by the rolling process, while compromising the material's plasticity, play a critical role in enhancing its strength. This is attributed to the increased barriers to dislocation motion provided by the dense twin structure and the strain hardening effect induced by the pre-deformation [39].

4. Discussion

During crystalline slip, partial dislocations bind carbon atoms on their slip planes. This process leads to a significant local increase in stacking fault energy (SFE). As C atoms are displaced into tetrahedral positions during the passage of a stacking fault, they attain an intermediate high-energy state conducive to interstitial C diffusion. Consequently, the subsequent migration of these C atoms to octahedral positions away from the stacking fault plane does not require the thermally activated overcoming of a high energy barrier typically associated with this intermediate state [40]. The passage of a dissociated dislocation effectively clears its glide plane of all initially present C atoms, thereby facilitating the glide of subsequent dislocations on the same plane, including those on cross-slip planes. This phenomenon enhances strain hardening by limiting dynamic recovery and promoting pronounced planar glide, as previously mentioned. The efficiency of this strain hardening mechanism is influenced by the stacking fault width, dislocation velocity, and the kinetics of C atom reorientation [15,25].

Figure 10 summarizes the deformation mechanisms of the two specimens in this study, namely 30Mn0.05C and 34Mn0.7C. During tensile deformation at LNT, the 30Mn0.05C steel undergoes stress-induced phase transformation from FCC austenite to HCP ε-martensite, driven by the combined effects of cryogenic conditions and the alloy's high-Mn/low-C composition, which reduces the SFE and destabilizes the austenitic matrix. This transformation-induced plasticity (TRIP) effect significantly enhances strength and work-hardening capacity through dynamic microstructural refinement and phase transformation strengthening, while the associated energy dissipation delays necking initiation [41]. Due to the controlled formation of a limited amount of ε-martensite, no embrittlement occurs, thereby preserving ductility. Consequently, the material exhibits an optimal combination of ultrahigh strength and high toughness.

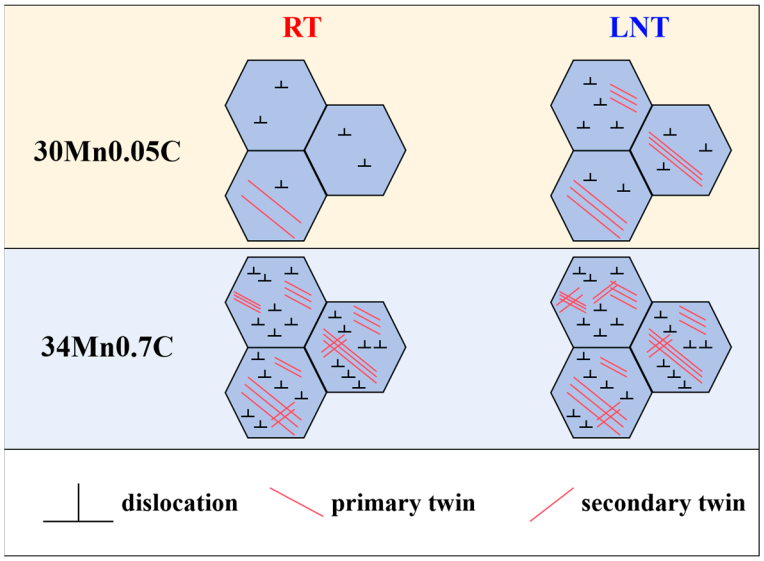


Figure 10. The schematic diagram showing the deformation mechanism of 30Mn0.05C and 34Mn0.7C at RT and LNT.

34Mn0.7C specimen exhibits a higher C content while maintaining a comparable grain size. During tensile deformation, the increased C content in 34Mn0.7C leads to a higher

density of dislocations. As deformation proceeds, a greater number of C diffuse into the moving dislocations, forming Mn-C complexes with Mn atoms [6,12]. These complexes exert a pinning effect on the dislocations, hindering their further slip. Consequently, the DSA effect is observed in 34Mn0.7C at RT, and this effect is more pronounced due to the higher C content. The stronger DSA effect enhances the work hardening rate, thereby improving both the strength and plasticity of the material.

In the tensile tests conducted on 34Mn0.7C at RT and LNT, the distinct behaviors observed in the strain curves can be attributed to the temperature-dependent activity of C atoms. At RT, C atoms in austenite retain sufficient mobility to diffuse into moving dislocations, increasing the likelihood of pinning effects on some dislocations. In contrast, at LNT, the decrease in temperature results in a reduction of the SFE, which promotes the occurrence of twinning. The deformation mechanism shifts from being predominantly dislocation slip to twinning, thereby reducing the interaction between dislocations and solute C atoms. This suppression of the DSA effect is primarily attributed to the alteration in the deformation mechanism. The change in the deformation mechanism is the main factor leading to the variation in the DSA effect.

Furthermore, the fully recrystallized specimen (34Mn0.7C-RT) and the rolled specimens with a lamellar structure (34Mn0.7C(L)-RT) exhibit varying degrees of the DSA effect, as shown in Figure 11. This difference is likely due to the introduction of a high density of dislocations and deformation twins in the 34Mn0.7C(L)-RT specimen during rolling deformation. During tensile deformation, most C atoms in 34Mn0.7C(L)-RT directly interact with pre-existing dislocations, inducing pinning effects without significant diffusion [42]. As a result, fewer C atoms participate in diffusion, leading to a weaker DSA effect in the rolled sample compared to the fully recrystallized one.

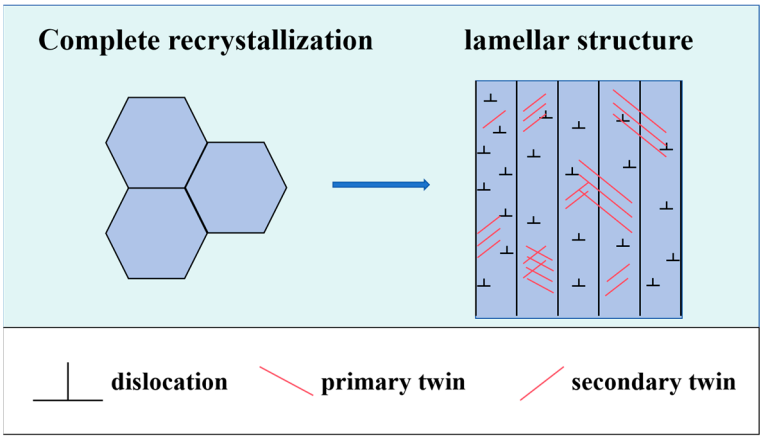


Figure 11. The schematic diagram showing the deformation mechanism of 34Mn0.7C(L).

The variation in twin area fraction observed in the two specimens exhibits a trend similar to that of dislocation density. This suggests that, with increasing C content, deformation twins become thinner and more densely distributed. The refinement and increased density of twins are closely associated with the enhanced interaction between dislocations and C atoms at higher C concentrations. Specifically, the intensified interaction between C and dislocations promotes the nucleation of deformation twins while simultaneously inhibiting their growth, leading to a reduction in twin thickness and inter-twin spacing [43]. A stronger DSA effect facilitates planar dislocation slip and amplifies local stress concentrations through dislocation pile-ups, which are conducive to the formation of deformation twins. Consequently, a stronger DSA effect is considered advantageous for increasing the twinning rate and contributes to the saturation of deformation twins in the 34Mn0.7C specimen during tensile deformation.

In addition to promoting deformation twinning, a stronger DSA effect also elevates dislocation density through mechanisms such as C segregation and planar dislocation slip at dislocation sites. Furthermore, twin boundaries act as potent barriers to dislocation motion, promoting dislocation accumulation and thereby increasing dislocation density [33]. The twin/matrix interfaces reduce the mean free path of dislocation motion, further contributing to the rise in dislocation density. Additionally, thinner twin layers accommodate fewer dislocations, necessitating higher external stress to drive dislocations across twin boundaries, which in turn increases dislocation density.

Therefore, the enhanced DSA effect shall lead to an increase in dislocation density. Then, twin boundaries act as favorable obstacles to dislocation motion, resulting in further accumulation of dislocations. These factors synergistically enhance the strain hardening capacity and mechanical properties.

5. Conclusions

In this study, we designed three specimens: 30Mn0.05C (fully recrystallized), 34Mn0.7C (fully recrystallized), and 34Mn0.7C(L) (lamellar structure). Tensile tests were conducted at RT and LNT conditions. Using various characterization techniques, the effects of C alloying, temperature, and microstructure on mechanical behavior and deformation mechanisms in high-manganese steels are examined. The main conclusions are as follows:

1. Increased C content enhances the DSA effect by increasing dislocation density and promoting Mn-C complex formation, which improves strength but reduces plasticity;
2. At LNT, the dominant deformation mechanism shifts from dislocation slip to twinning, driving changes in DSA behavior;
3. The DSA effect is stronger in fully recrystallized specimens than in lamellar structures due to pre-existing dislocations and deformation twins that limit C atom diffusion.

Author Contributions: Conceptualization, Y.W. and C.Z. (Chenghao Zhang); methodology, Y.W., C.Z. (Chenghao Zhang), T.Z., J.Z., C.Z. (Chunlei Zheng), L.K. and H.Y.; validation, Y.W., H.Y., T.Z., J.Z., C.Z. (Chenghao Zhang) and C.Z. (Chunlei Zheng); investigation, L.K., T.Z., J.Z. and C.Z. (Chenghao Zhang); data curation, C.Z. (Chenghao Zhang), C.Z. (Chunlei Zheng), T.Z., L.K. and J.Z.; writing—original draft preparation, C.Z. (Chenghao Zhang); writing—review and editing, Y.W., C.Z. (Chenghao Zhang), T.Z., J.Z., H.Y., L.K. and C.Z. (Chunlei Zheng); funding acquisition Y.W. All authors have read and agreed to the published version of the manuscript.

Funding: The research was funded by the Central Government Guidance Fund for Local Science and Technology (226Z1003G) and the National Key Research and Development Program (2022YFB3705500).

Data Availability Statement: Data will be made available on request.

Conflicts of Interest: The authors declare no conflict of interest.

References

1. Fu, P.; Zheng, Z.B.; Yang, W.P.; Yang, H.K. Influence of carbon addition on mechanical properties of Fe-Mn-C twinning-induced plasticity steels. *J. Iron Steel Res. Int.* **2022**, *29*, 1446–1454. [CrossRef]
2. Qi, X.Y.; Chen, C.; Li, Y.G.; Yang, Z.N.; Shen, S.C.; Lv, B.; Zhang, F.C. Flow softening behavior associated with dynamic recrystallization and preferential growth of a multielement strengthening high-Mn austenitic steel. *J. Iron Steel Res. Int.* **2025**. [CrossRef]
3. Koyama, M.; Sawaguchi, T.; Tsuzaki, K. Overview of Dynamic Strain Aging and Associated Phenomena in Fe-Mn-C Austenitic Steels. *ISIJ Int.* **2018**, *58*, 1383–1395. [CrossRef]
4. Oh, S.-K.; Kwon, H.-J.; Lee, Y.-K. Reconsideration of the dislocation arrest model for dynamic strain aging in C-bearing high Mn steel with low stacking fault energy. *Mater. Sci. Eng. A* **2024**, *897*, 146304. [CrossRef]

5. Yang, H.K.; Zhang, Z.J.; Tian, Y.Z.; Zhang, Z.F. Negative to positive transition of strain rate sensitivity in Fe-22Mn-0.6C-x(Al) twinning-induced plasticity steels. *Mater. Sci. Eng. A* **2017**, *690*, 146–157. [CrossRef]
6. Nam, J.-H.; Oh, S.-K.; Park, M.-H.; Lee, Y.-K. The mechanism of dynamic strain aging for type A serrations in tensile curves of a medium-Mn steel. *Acta Mater.* **2021**, *206*, 116613. [CrossRef]
7. Yilmaz, A. The Portevin–Le Chatelier effect: A review of experimental findings. *Sci. Technol. Adv. Mater.* **2011**, *12*, 063001. [CrossRef]
8. McCormick, P.G. The Portevin-Le Chatelier effect in a pressurized low carbon steel. *Acta Metall.* **1973**, *21*, 873–878. [CrossRef]
9. Cottrell, A.H. LXXXVI. A note on the Portevin-Le Chatelier effect. *Lond. Edinb. Dublin Philos. Mag. J. Sci.* **1953**, *197*, 829–832. [CrossRef]
10. Caillard, D. Dynamic strain ageing in iron alloys: The shielding effect of carbon. *Acta Mater.* **2016**, *112*, 273–284. [CrossRef]
11. Van den Beukel, A. Theory of the effect of dynamic strain aging on mechanical properties. *Phys. Stat. Solidi (a)* **1975**, *30*, 197–206. [CrossRef]
12. Hwang, S.; Park, M.-H.; Bai, Y.; Lavakumar, A.; Shibata, A.; Adachi, H.; Sato, M.; Tsuji, N. Mechanism of DSA effect correlating to the macroscopic PLC banding in high-Mn austenitic steel. *Scr. Mater.* **2024**, *249*, 1359–6462. [CrossRef]
13. Yang, H.K.; Tian, Y.Z.; Zhang, Z.J.; Zhang, P.; Zhang, Z.F. Temperature-Dependence of the Mechanical Responses for Two Types of Twinning-Induced Plasticity Steels. *Metall. Mater. Trans. A* **2018**, *49*, 1475–1480. [CrossRef]
14. Yang, H.K.; Tian, Y.Z.; Zhang, Z.F. Dramatic Increase of Strength and Ductility in Fe-22Mn-1.0C Twinning-Induced Plasticity Steel at Elevated Temperature. *Adv. Eng. Mater.* **2019**, *21*, 1438–1656. [CrossRef]
15. Lee, S.-J.; Kim, J.; Kane, S.N.; De Cooman, B.C. On the origin of dynamic strain aging in twinning-induced plasticity steels. *Acta Mater.* **2011**, *59*, 6809–6819. [CrossRef]
16. Grässel, O.; Krüger, L.; Frommeyer, G.; Meyer, L.W. High strength Fe-Mn-(Al, Si) TRIP/TWIP steels development-properties-application. *Int. J. Plast.* **2000**, *16*, 1391–1409. [CrossRef]
17. Madivala, M.; Schwedt, A.; Wong, S.L.; Roters, F.; Prahl, U.; Bleck, W. Temperature dependent strain hardening and fracture behavior of TWIP steel. *Int. J. Plast.* **2018**, *104*, 80–103. [CrossRef]
18. Renard, K.; Ryelandt, S.; Jacques, P.J. Characterisation of the Portevin-Le Châtelier effect affecting an austenitic TWIP steel based on digital image correlation. *Mater. Sci. Eng. A* **2010**, *527*, 2969–2977. [CrossRef]
19. Litovchenko, I.; Akkuzin, S.; Polekhina, N.; Spiridonova, K.; Osipova, V.; Kim, A.; Moskvichev, E.; Chernov, V.; Kuznetsov, A. Microstructure Features and Mechanical Properties of Modified Low-Activation Austenitic Steel in the Temperature Range of 20 to 750 °C. *Metals* **2023**, *13*, 2015. [CrossRef]
20. Khedr, M.; Li, W.; Min, N.; Liu, W.; Jin, X. Effects of increasing the strain rate on mechanical twinning and dynamic strain aging in Fe-12.5Mn-1.1C and Fe–24Mn-0.45C–2Al austenitic steels. *Mater. Sci. Eng. A* **2022**, *842*, 143024. [CrossRef]
21. Seol, J.B.; Kim, J.G.; Na, S.H.; Park, C.G.; Kim, H.S. Deformation rate controls atomic-scale dynamic strain aging and phase transformation in high Mn TRIP steels. *Acta Mater.* **2017**, *131*, 187–196. [CrossRef]
22. Saeed-Akbari, A.; Mishra, A.K.; Mayer, J.; Bleck, W. Characterization and Prediction of Flow Behavior in High-Manganese Twinning Induced Plasticity Steels: Part II. Jerky Flow and Instantaneous Strain Rate. *Metall. Mater. Trans. A* **2012**, *43*, 1705–1723. [CrossRef]
23. Lee, S.-Y.; Lee, S.-I.; Hwang, B. Effect of strain rate on tensile and serration behaviors of an austenitic Fe-22Mn-0.7C twinning-induced plasticity steel. *Mater. Sci. Eng. A* **2018**, *711*, 22–28. [CrossRef]
24. Liang, Z.Y.; Wang, X.; Huang, W.; Huang, M.X. Strain rate sensitivity and evolution of dislocations and twins in a twinning-induced plasticity steel. *Acta Mater.* **2015**, *88*, 170–179. [CrossRef]
25. De Cooman, B.C.; Estrin, Y.; Kim, S.K. Twinning-induced plasticity (TWIP) steels. *Acta Mater.* **2018**, *142*, 283–362. [CrossRef]
26. Koyama, M.; Sawaguchi, T.; Tsuzaki, K. Deformation Twinning Behavior of Twinning-induced Plasticity Steels with Different Carbon Concentrations—Part 2: Proposal of Dynamic-strain-aging-assisted Deformation Twinning. *ISIJ Int.* **2015**, *55*, 1754–1761. [CrossRef]
27. Oh, S.-K.; Kilic, M.E.; Seol, J.-B.; Hong, J.-S.; Soon, A.; Lee, Y.-K. The mechanism of dynamic strain aging for type A serrations in tensile flow curves of Fe-18Mn-0.55C (wt.%) twinning-induced plasticity steel. *Acta Mater.* **2020**, *188*, 366–375. [CrossRef]
28. Otto, F.; Dlouhý, A.; Somsen, C.; Bei, H.; Eggeler, G.; George, E.P. The influences of temperature and microstructure on the tensile properties of a CoCrFeMnNi high-entropy alloy. *Acta Mater.* **2013**, *61*, 5743–5755. [CrossRef]
29. Chen, S.; Xie, X.; Li, W.; Feng, R.; Chen, B.; Qiao, J.; Ren, Y.; Zhang, Y.; Dahmen, K.A.; Liaw, P.K. Temperature effects on the serrated behavior of an Al0.5CoCrCuFeNi high-entropy alloy. *Mater. Chem. Phys.* **2018**, *210*, 20–28. [CrossRef]
30. Zhang, Y.; Liu, J.P.; Chen, S.Y.; Xie, X.; Liaw, P.K.; Dahmen, K.A.; Qiao, J.W.; Wang, Y.L. Serration and noise behaviors in materials. *Prog. Mater. Sci.* **2017**, *90*, 358–460. [CrossRef]
31. Wang, Y.; Zhang, Y.; Godfrey, A.; Kang, J.; Peng, Y.; Wang, T.; Hansen, N.; Huang, X. Cryogenic toughness in a low-cost austenitic steel. *Commun. Mater.* **2021**, *2*, 44. [CrossRef]

32. Koyama, M.; Shimomura, Y.; Chiba, A.; Akiyama, E.; Tsuzaki, K. Room-temperature blue brittleness of Fe-Mn-C austenitic steels. *Scr. Mater.* **2017**, *141*, 20–23. [CrossRef]
33. Xiong, J.; Liu, E.; Zhang, C.; Kong, L.; Yang, H.; Zhang, X.; Wang, Y. Tuning mechanical behavior and deformation mechanisms in high-manganese steels via carbon content modification. *Mater. Sci. Eng. A* **2023**, *881*, 145401. [CrossRef]
34. Dini, G.; Ueji, R.; Najafizadeh, A.; Monir-Vaghefi, S.M. Flow stress analysis of TWIP steel via the XRD measurement of dislocation density. *Mater. Sci. Eng. A* **2010**, *527*, 2759–2763. [CrossRef]
35. Jeong, K.; Jin, J.-E.; Jung, Y.-S.; Kang, S.; Lee, Y.-K. The effects of Si on the mechanical twinning and strain hardening of Fe–18Mn–0.6C twinning-induced plasticity steel. *Acta Mater.* **2013**, *61*, 3399–3410. [CrossRef]
36. Hutchinson, B.; Ridley, N. On dislocation accumulation and work hardening in Hadfield steel. *Scr. Mater.* **2006**, *55*, 299–302. [CrossRef]
37. Mohammadzadeh, R.; Mohammadzadeh, M. Inverse grain size effect on twinning in nanocrystalline TWIP steel. *Mater. Sci. Eng. A* **2019**, *747*, 265–275. [CrossRef]
38. Koyama, M.; Lee, T.; Lee, C.S.; Tsuzaki, K. Grain refinement effect on cryogenic tensile ductility in a Fe-Mn-C twinning-induced plasticity steel. *Mater. Des.* **2013**, *49*, 234–241. [CrossRef]
39. Wang, Y.; Kang, J.; Peng, Y.; Wang, T.; Hansen, N.; Huang, X. Laminated Fe-34.5 Mn-0.04C composite with high strength and ductility. *J. Mater. Sci. Technol.* **2018**, *34*, 1939–1943. [CrossRef]
40. Sun, S.; Xue, Z. Effect of Aging Process on the Strain Rate Sensitivity in V-Containing TWIP Steel. *Metals* **2021**, *11*, 126. [CrossRef]
41. Li, S.; Withers, P.J.; Kabra, S.; Yan, K. The behaviour and deformation mechanisms for 316L stainless steel deformed at cryogenic temperatures. *Mater. Sci. Eng. A* **2023**, *880*, 145279. [CrossRef]
42. Wang, Y.H.; Kang, J.M.; Peng, Y.; Wang, T.S.; Hansen, N.; Huang, X. Hall-Petch strengthening in Fe-34.5Mn-0.04C steel cold-rolled, partially recrystallized and fully recrystallized. *Scr. Mater.* **2018**, *155*, 41–45. [CrossRef]
43. Steinmetz, D.R.; Jäpel, T.; Wietbrock, B.; Eisenlohr, P.; Gutierrez-Urrutia, I.; Saeed, A.; Hickel, T.; Roters, F.; Raabe, D. Revealing the strain-hardening behavior of twinning-induced plasticity steels: Theory, simulations, experiments. *Acta Mater.* **2013**, *61*, 494–510. [CrossRef]

Disclaimer/Publisher's Note: The statements, opinions and data contained in all publications are solely those of the individual author(s) and contributor(s) and not of MDPI and/or the editor(s). MDPI and/or the editor(s) disclaim responsibility for any injury to people or property resulting from any ideas, methods, instructions or products referred to in the content.